AMERICAN ACADEMY
OF OPHTHALMOLOGY®

In partnership with the

AMERICAN
GLAUCOMA
SOCIETY

Concordance of Objectively Detected Retinal Nerve Fiber Bundle Defects in En Face OCT Images with Conventional Structural and Functional Changes in Glaucoma

Riccardo Cheloni, PhD, Jonathan Denniss, PhD

Purpose: To assess how objectively detected defects in retinal nerve fiber bundle (RNFB) reflectance on en face OCT images relate to circumpapillary retinal nerve fiber layer thickness (cpRNFLT) and visual field defects.

Design: Cross-sectional study.

Participants: Sixteen participants with early glaucoma and 29 age-matched healthy controls, of whom 22 had usable en face images for the establishment of normative levels of RNFB reflectance.

Methods: All the participants underwent cpRNFLT scans, visual field examination, and wide-field OCT. En face reflectivity was assessed objectively using the Summary of Multiple Anatomically Adjusted Slabs method. En face defects were deemed concordant with cpRNFLT when they had at least 1 cpRNFLT point with $P < 0.01$, within $\pm 15°$ of the predicted insertion on the optic disc. Visual fields were examined using custom suprathreshold perimetry and SITA Standard 24-2. For each visual field location, the corresponding reflectance was deemed abnormal if any en face superpixel within $\pm 1°$ was abnormal. The overall, positive, and negative agreements were measured in each participant.

Main Outcome Measures: Proportion of concordant defects between en face reflectance analysis and cpRNFLT (%) as well as overall, positive, and negative agreements between en face reflectance analysis and visual field results.

Results: Most en face abnormalities had concordant cpRNFLT defects in the mapped sector (median proportion concordant, 0.85; interquartile range, 0.74–0.95). In eyes with glaucoma, a median of 8.1% (range, 2.4%–23.7%) and 14.9% (range, 3.5%–29.1%) locations showed corresponding en face and visual field defects using 24-2 and custom perimetry, respectively. Both the perimetric strategies had moderate-to-good raw agreement with en face analysis (0.66–0.68), with stronger agreement on normal findings than on defects (0.77–0.78 and 0.4–0.44).

Conclusions: Objectively extracted reflectance defects showed strong concordance with conventional cpRNFLT damage and good agreement with perimetry, which could be enhanced by further minimization of image artifacts. *Ophthalmology Glaucoma 2022;■:1–15 © 2022 by the American Academy of Ophthalmology. This is an open access article under the CC BY license (http://creativecommons.org/licenses/by/4.0/).*

Supplemental material available at www.ophthalmologyglaucoma.org.

OCT is becoming increasingly valuable in the assessment of glaucoma.[1,2] Although OCT has brought significant support to clinicians in the diagnostic process,[3] detection of early cases through cross sectional examination continues to be challenging.[4–7] As such, there remains a strong rationale for developing methods for improved diagnosis of glaucoma.

En face OCT imaging is a relatively new approach to examine structural damage in eyes with glaucoma.[8–11] The technique enables the assessment of retinal nerve fiber bundle (RNFB) reflectance and is performed using dense volumetric scans of the retinal area of interest. The intensity of each A-scan over a certain range of depths is then averaged into a 2-dimensional image,[8,9,12,13] resulting in a transverse retinal section, or slab, derived from varying retinal thicknesses.[9,12] Defects on en face OCT images appear as hyporeflective regions, likely because of a combination of primary loss of RNFB reflectance and thinning of the retinal nerve fiber layer (RNFL).[8,9] En face imaging holds promise in glaucoma assessment because evidence from animal models has suggested that loss of RNFL reflectivity may precede measurable thickness changes, suggesting a potential use in early detection of glaucoma.[14–16] Additionally, slab images generated with

this modality enable a direct topographic relationship between structural changes and visual field measures.[17,18] This facilitates the assessment of structure—function relationships independently from maps that relate the visual field to the optic nerve head (ONH), removing 1 source of error.[19]

Studies of en face OCT have suggested that changes in RNFB reflectance have a strong relationship with conventional circumpapillary retinal nerve fiber layer (cpRNFL) thickness (cpRNFLT) analyses.[8,11] Good correspondence with visual field loss has also been reported.[12,18,20,21] However, reflectance changes in most studies have been evaluated subjectively by clinicians, as has the relationship between en face abnormalities and other tests such as cpRNFL and visual field analyses. Indeed, the novelty of en face OCT analysis of eyes with glaucoma means there is currently a lack of widely accepted objective methods for defining defects.[22]

We recently introduced Summary of Multiple Anatomically-adjusted Slabs (SMAS), a novel method for automated and objective extraction of RNFB reflectance defects in en face images.[23] To further validate SMAS, this study aimed to assess how extracted en face findings relate to more conventional measures of glaucoma: structural changes in cpRNFLT and visual field loss in eyes with early-to-moderate glaucoma.

Methods

The study was performed in accordance with the tenets of the Declaration of Helsinki and received ethical approval from the National Health Service Research Ethics Service. All participants provided written informed consent to participate.

Participants

This cross sectional study included participants with glaucoma with early-to-moderate vision loss, defined as a standard automated perimetry (SAP) mean deviation (MD) of better than −8 dB, and age-matched healthy controls. The participants underwent eye examinations, including refraction, slit-lamp examination, Goldmann applanation tonometry, and SAP (24-2 SITA Standard, Humphrey Field Analyzer III; Carl Zeiss Meditec Inc). Spectral-domain OCT imaging was performed using Spectralis (Heidelberg Engineering) and included an analysis of the ONH and macula, enabling automated localization of the fovea and the center of the ONH. Circumpapillary retinal nerve fiber layer thickness data along a 3.5-mm-diameter circular scan were also extracted. The participants also underwent dense OCT imaging of the central retina, allowing us to extract en face images, and a custom perimetry test, the details of which are provided below.

For inclusion, participants with glaucoma required a consultant ophthalmologist-performed diagnosis of open-angle glaucoma and evidence of structural damage, defined as at least 1 abnormal sector ($P < 0.01$) in the Spectralis cpRNFL analysis. No criteria based on visual field defects were required for inclusion in the glaucoma group; this enabled the inclusion of participants with a structural defect and no measurable visual field defect detected using SAP 24-2. Participants with any other eye conditions except glaucoma were excluded. Age-matched healthy controls were included if they had no disease affecting their visual system and had a normal visual field, as defined by a normal MD ($P > 0.05$); Glaucoma Hemifield Test within normal limits; and the absence of 3 contiguous non-edge points with $P < 0.05$ on the Pattern Deviation plot. Additional inclusion criteria for all participants were a refractive error magnitude of < 6.00 diopter sphere or 3.00 diopter cylinder and clear ocular media[24] or a history of uncomplicated cataract surgery. Only 1 eye per participant was included. In cases in which both eyes were eligible, the tested eye was selected at random in the healthy controls, whereas the one with the milder defect (less negative MD) was included in the group of participants with glaucoma.

En Face Defects of RNFB Reflectivity

The details of OCT imaging and en face slab extraction have been presented previously.[11,22,23] Compared with our previous work, data from 3 additional healthy eyes were available for inclusion to establish normative data.[23] We collected multiple dense OCT scans over the central $\pm 25°$ of the retina, and reflectivity data were extracted as single pixel slabs (3.87 μm) containing depth-resolved attenuation coefficients.[25] Single slabs were montaged and combined according to the SMAS method, as described in detail elsewhere.[23] For each participant, SMAS constructed seven 16-μm-thick en face slabs, overall encompassing retinal depths of 8 to 116 μm below the inner limiting membrane. Reflectivity is evaluated on a superpixel grid by comparing individual findings with normative data from age-matched controls. Superpixels with $P < 0.01$ of normative reflectivity were considered as defects when they occurred in any slab (i.e., at any depth). To assess reflectivity only at locations with expected RNFBs in healthy retinae, regions with normative reflectivity of ≥ 2.5 standard deviation (SD) below the mean intensity of visible bundles were censored from analysis at each depth. To account for individual differences in anatomy, all slab images were adjusted for the participant's fovea—disc and fovea—raphe angles using geometric transformations (double-shear transformation, Fig 1). Further, superpixel dimensions were individually adjusted to have a fixed number of superpixels (20) separating the fovea and the center of the ONH in all tested eyes (Fig 1). This method results in more defects being detected in more superficial slabs and the number of new defects that were not detected in more superficial slabs decreasing with increasing slab depth (Table S1, available at www.ophthalmologyglaucoma.org).

Deviation maps generated using SMAS were first back transformed to the original retinal configuration of each individual eye. Subsequently, the deviation maps were converted from superpixels to degrees using the estimated ONH location in degrees as extracted from the Spectralis software (see Fig 1 for an example). Superpixels had a median diameter of $0.7°$ (range, $0.67°–0.85°$).

Circumpapillary RNFL Defects

To identify cpRNFLT abnormalities, we compared the measurements of each eye with glaucoma with age-adjusted normative data from healthy controls. Circumpapillary retinal nerve fiber layer thickness measurements, automatically segmented by the device software, were extracted from Spectralis after verification of segmentation by 1 of the authors (R.C.). Data from all participants were first adjusted for the individual fovea—disc angle, automatically measured using Spectralis, setting $0°$ at the fovea—disc axis. The thickness measurements at different angular locations in the controls were consistent with normal distributions, as evaluated by visualization of histograms and Shapiro—Wilk tests (all $P > 0.05$). When normative cpRNFLT data were determined, age was the only covariate for which data were adjusted, as per current clinical practice.[26] Because our sample size for linear regression was limited,[27] pointwise estimates of age-related changes in cpRNFLT (μm/yr)
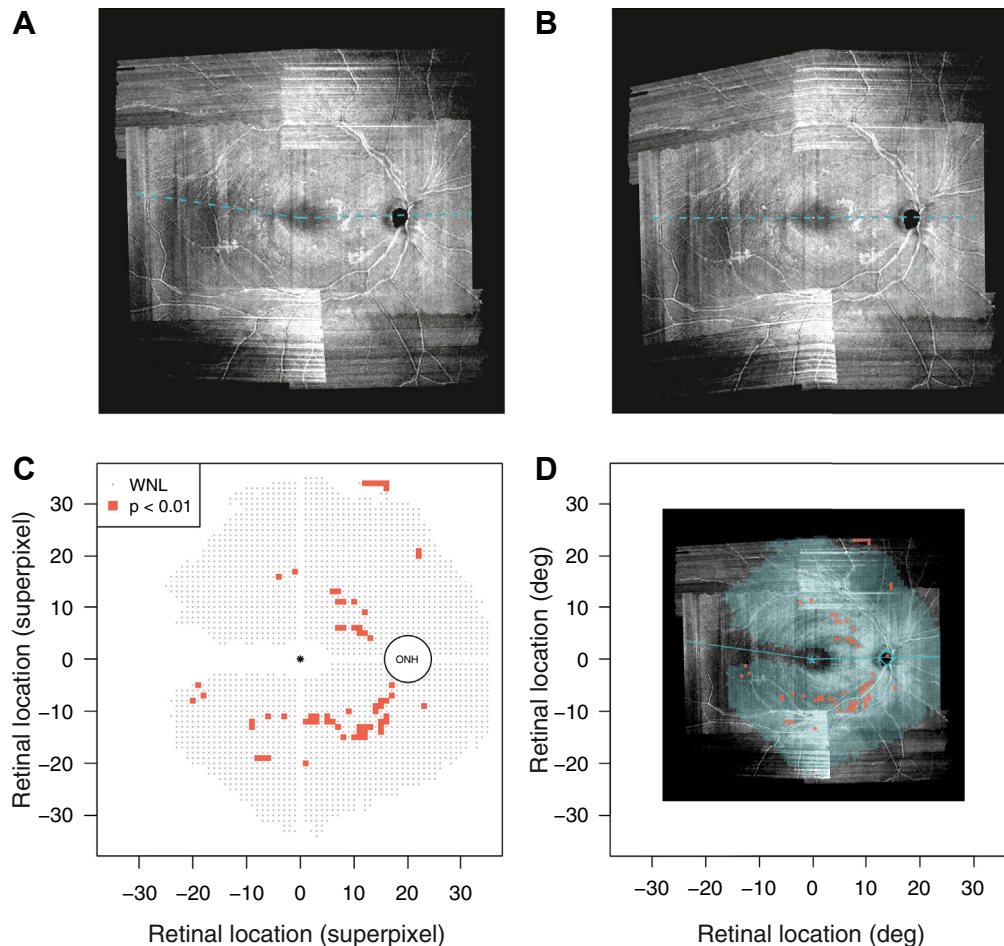
Figure 1. Example of double-shear transformation applied within Summary of Multiple Anatomically-adjusted Slabs and conversion from superpixels to degrees for 1 eye with glaucoma. **A,** An original en face image (8–23 μm below the inner limiting membrane); the blue dashed lines represent fovea–raphe and fovea–disc angles. **B,** An image transformed according to Summary of Multiple Anatomically-adjusted Slabs—raphe, fovea and optic nerve head are aligned on a common horizontal axis. **C,** Summary of Multiple Anatomically-adjusted Slabs deviation map. **D,** The map converted from superpixels to degrees and transformed back to the original retinal configuration (1 superpixel = 0.68°). deg = degree; ONH = optic nerve head; WNL = within normal limits.

were extracted from a population-based study that evaluated a large cohort of healthy eyes using the same OCT device and scan pattern adopted here.[28] The difference between individual participants' age and the average age of our controls was first computed and used to identify correcting factors at each of 768 cpRNFLT points. These values were then used to correct normative cpRNFLT in our controls at all angular locations. The lower limit of normality of cpRNFLT in our controls was set at $P < 0.01$. This was computed by subtracting 2.33 SDs from the mean thickness of the healthy controls at each of the 768 points after age adjustment.

Finally, to facilitate the analysis of correspondence with en face defects and support the required mapping arrangements (see below), individual deviation maps were rotated by their fovea–disc angle. This allowed us to set 0° temporally, consistent with the structure–function map used to project en face defects at the ONH.

Visual Field Examination

Within 30 days of OCT imaging, the participants underwent SAP (24-2, SITA Standard) and a dense suprathreshold custom perimetry test, implemented via the Open Perimetry Interface[29] on the

Octopus 900 perimeter (Haag-Streit AG). The details of custom perimetry are reported in Table S1 (available at www.ophthalmologyglaucoma.org). In brief, this perimetric strategy considered 643 locations over the 24-2 grid limits (Fig 1A), with 1° density in the central 10° and 2° density in the midperiphery. Goldmann size III (diameter, 0.43°) stimuli were used, with the intensity selected according to age-adjusted and location-specific normative sensitivities.[30] To increase the specificity of defect detection in spite of a potentially reduced sensitivity,[31,32] stimuli of 2 SDs plus 2 dB below the age-adjusted normative sensitivity were presented at each location.

For both the perimetric procedures, only reliable tests were included, assessed via a subjective observation of fixation stability using an internal fixation monitor[33] and reliability indices (false positives, false negatives, and fixation losses) of $< 20\%$ in the SAP test.

Custom perimetry provides a dichotomous classification of any visual field location as normal or defective. Accordingly, the SAP results were also dichotomized. For consistency with en face analysis and custom perimetry, the total deviation values were evaluated. The cutoff used to define visual field defects in custom
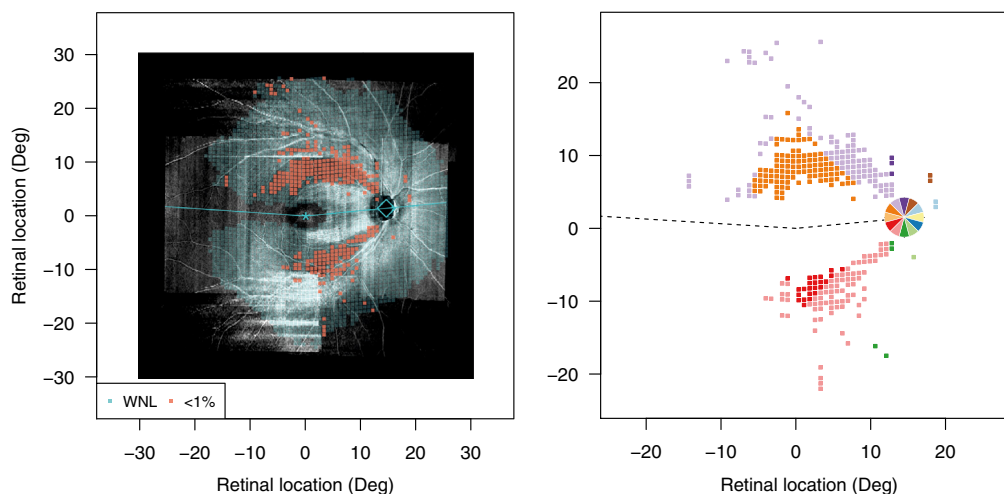
Figure 2. Example of the mapping model used in this study to relate en face reflectance defects to angular locations around the optic disc in a participant with glaucoma. The left plot shows the Summary of Multiple Anatomically-adjusted Slabs deviation map overlaid on an en face image of the corresponding eye. In the right plot, en face defects are color coded according to the angular location of insertion around the optic nerve head, in 30° sectors. Deg = degree; WNL = within normal limits.

perimetry (2 SDs and 2 dB below the mean) approximately corresponds to $P < 0.023$. Accordingly, SAP locations were deemed abnormal when the total deviation had $P < 0.02$.

Structure–Structure and Structure–Function Maps

To map reflectance defects on the en face images to corresponding angular locations around the ONH, we used a computational model for structure–function that can produce mapping specific for individual anatomy of the eye tested.[34–38] The model is customized to individual participants' ONH location and disc–fovea–raphe angle, measured on the en face images. The model allowed us to map any location in the retina to specific angles on the ONH.[34] Individualized maps were extracted specific to each participant's en face deviation map, identifying the corresponding angles of insertion on the cpRNFL profile for each abnormal superpixel (Fig 2).

To explore the relationship between en face reflectivity and visual function, visual field locations were corrected for retinal ganglion cell (RGC) displacement according to the model proposed by Drasdo et al.[39] No correction was applied to en face OCT data.

Analysis

En face OCT images are subject to artifacts arising from many sources, including low-quality B-scans, floaters, and glial cell alterations.[40] The impact of artifacts on slab images was examined by 2 investigators (R.C. and J.D.), and in case of substantial impact, either whole images or specific regions were excluded from further analysis. Each case was jointly discussed by the authors until a consensus on data exclusion was reached. To facilitate comparison and reporting, all en face deviation maps and visual field data were transformed into right eye retina view format. En face defects within a 2° radius of the center of the ONH were excluded from the analysis because these are likely to fall within the ONH or on its margins.

To explore the relationship between reflectance defects and cpRNFLT loss (structure–structure), we considered recommendations of a recently proposed framework to assess concordance between changes in the retina and at the optic disc.[38] Accordingly, we noted that healthy locations in the central retina could project to abnormal cpRNFL sectors. Axons from peripheral damaged retina might also

enter the ONH at similar angular locations (i.e., peripheral damage and intact central retina), ultimately leading to cpRNFL defects. Hence, analyses should focus on damaged retinal locations, which should also constitute the starting point in the examination of this relationship. We considered structure–structure to be concordant when the 30° sector centered on the predicted angle of insertion on the ONH of any en face defect presented at least 1 abnormal cpRNFLT point ($P < 0.01$). The 30° sector ($\pm 15°$ on the predicted angle) was selected according to estimates of mapping variability, as defined by measurement errors of parameters seeding custom structure–function mapping.[35,37] For each participant, an overall measure of topographic concordance was computed as the concordance ratio, which was the proportion of concordant defects among all en face defects. Bootstrapped 95% confidence intervals (CIs) were also computed (n = 1000 resampling).

Second, we explored the level of agreement between en face defects in reflectance and corresponding visual function in perimetry (structure–function). Consistent with the structure–structure analysis, sources of variability within structure–function mapping were considered by allowing a $\pm 1°$ tolerance level in the evaluation of concordance. This tolerance level was chosen to account for the effects of fixation instability and differences between the fovea and the preferred retinal locus for fixation[41,42] as well as errors in RGC displacement models.[19,39,43] As such, structure–function agreement was established between any visual field location and en face superpixels lying within 1° (Fig 3). Only en face superpixels with the nearest displaced visual field location within 1° were considered and used to generate a dichotomous prediction of visual field status. Similarly, visual field locations with no en face superpixels within the tolerance distance were ignored. Function was predicted to be abnormal if at least 1 superpixel was found to be abnormal within the relevant cluster of each visual field location for both SAP and custom perimetry.

Unlike the evaluation of the structure–structure relationship, the analysis of concordance between en face findings and corresponding function considered both defects and healthy regions. As a general measure of concordance, we used overall raw agreement (equation 1) and tetrachoric correlation,[44,45] which were computed individually for each eye. The tetrachoric correlation was computed using the Correlation package in R[46] and provides ρ coefficients between 2 dichotomous variables. Unlike K statistics,
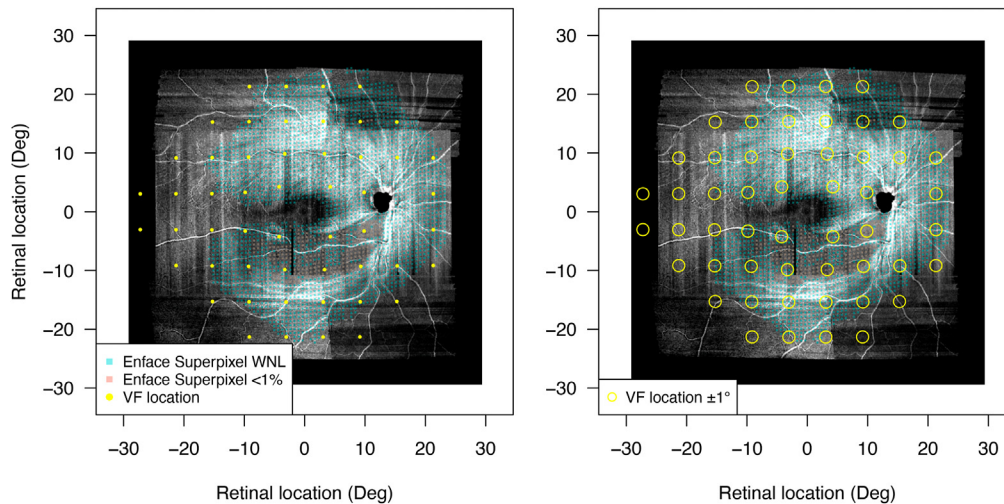
Figure 3. Example of tolerance level considered in the analysis of structure—function agreement between en face reflectance and visual function in standard automated perimetry. The left image shows displaced visual field grids in Goldmann size III stimuli on an en face image and deviation map. The right image shows the same 24-2 locations, including the ± 1° tolerance level around visual field locations (yellow circles). Visual field locations with no en face superpixels within ± 1° were excluded from analysis. Deg = degree; VF = visual field; WNL = within normal limits.

tetrachoric correlation is not affected by the marginal proportions of rating levels[47] and has the advantage of providing a familiar effect size.

To provide insights into differential agreement from positive and negative ratings, positive and negative conditional agreements were also computed. Positive agreement represents the conditional probability that a test shows a defect when the location is defective on another test. Similarly, negative agreement measures the probability of a concordant measure of normality. The 2 measures of agreement are adjusted for chance and uneven distributions of ratings (i.e., prevalence) across different individuals.[48] Equations 2 and 3 were used:[48,49]

$$\text{Overall raw agreement} = [a + d] / N \qquad (1)$$

$$\text{Positive agreement} = 2a / [2a + b + c] \qquad (2)$$

$$\text{Negative agreement} = 2d / [2d + b + c] \qquad (3)$$

where "a" represents the number of defects detected in both the domains, "b" represents the number of en face defects matched by normal findings in perimetry, "c" represents the number of normal en face findings matched by perimetric defects, "d" represents the number of normal findings in both the domains, and "N" represents the total number of locations considered in a given participant.

For each participant, the estimates of overall, positive, and negative agreements were computed alongside their bootstrapped 95% CI. Fisher's exact test was used to test the independence of the 2 test modalities.[47] The overall measures of correlation were provided as median and range, with the median computed after transformation of correlation coefficients to Z values and then back to correlation coefficients.

Results

Overall, 29 controls were included, of whom 22 had usable en face images for the establishment of normative levels of RNFB reflectance. Among 21 participants with early-to-moderate glaucoma imaged using en face OCT, 5 participants (median age, 69 years; range, 67—78; median MD, −4.8 dB; range, −6.1 to −1.6 dB)

were excluded because of substantial artifacts affecting the final images. A part of the images of 3 additional participants with glaucoma was censored for similar reasons. Overall, findings from 16 participants with glaucoma were included in the analysis; their demographics are reported in Table 1. All the participants with glaucoma, except 1, presented with a visual field defect, determined based on the criteria used for the inclusion of healthy controls. The remaining eye had 3 contiguous defective points, but 1 was an edge location. In the structure—function concordance analysis, visual field defects were considered when the total deviation had P < 0.02. Compared with the alternative of using pattern deviation with P < 0.02, in our sample, the visual fields dichotomized in this way had strong agreement (median, 0.942; interquartile range [IQR], 0.923−1) and correlation (median ρ,

Table 1. Demographics and Clinical Characteristics of Included Participants*

	Controls (n = 29)		Glaucoma (n = 16)
	cpRNFL Norms (n = 29)	En Face Norms (n = 22)	
Age, yrs	69 (8.0)	67.5 (4.0)	70 (8.3)
Eye			
Right	15	14	4
Left	14	8	12
Ethnicity			
White British	28	21	16
Other	1	1	0
Global cpRNFLT, μm	97 (14)	97.5 (11.5)	68 (14)
SAP MD, dB	0.5 (1.4)	0.8 (1.4)	−3.3 (2.2)
Axial length, mm	23.5 (0.7)	23.3 (0.6)	24.05 (0.95)

cpRNFL = circumpapillary retinal nerve fiber layer; cpRNFLT = circumpapillary retinal nerve fiber layer thickness; dB = decibels; MD = mean deviation; SAP = standard automated perimetry.
*Continuous data are summarized as median (interquartile range).

0.969; IQR, 0.959−0.989) and had a median of only 3 locations with a different status between the methods.

Structure−Structure Concordance

Among the participants with glaucoma, out of 2492 superpixels tested on average (∼ 12.9%), a median of 322 abnormal superpixels (IQR, 181−463) were identified in each eye. The objectively extracted reflectance defects showed strong concordance with conventional cpRNFL thinning (median concordance ratio, 0.85; IQR, 0.74−0.95). On average, 85% of en face defects in this sample had a cpRNFL location with thickness with $P < 0.01$ within ± 15° of the predicted insertion on the ONH.

Figure 4 shows the details of concordance for each individual eye. The smallest concordance ratio was 0.48 (95% CI, 0.36−0.6; participant 1; Fig 4), whereas the eye showing the highest concordance ratio between en face reflectance analysis and cpRNFLT was participant 13 (0.99; 95% CI, 0.99−1.0), in which nearly all en face reflectance defects matched with thinned cpRNFL.

The distributions of en face angular projections on the ONH are shown in Figure 5, and en face defects most frequently mapped to the superior temporal (40°−50°) and inferior temporal (300°) aspects of the ONH. Concordant en face defects were found slightly further away from the ONH compared with nonconcordant defects (median, 15.2°; IQR, 14.5−17 vs. median, 13.4°; IQR, 10.2−15.8; paired *t* test, $P = 0.006$).

Structure−Function Concordance (Custom Perimetry and SAP)

The analysis of SAP results was limited to 15 eyes with glaucoma because 1 of the participants (participant 16) had abnormal locations only in the nasal step area, where no en face predictions were made (see Fig 3 for example). The tolerance level selected in the structure−function agreement analysis led to a median of 5.8 (IQR, 5.5−6.1) superpixels being considered in each cluster used to make a prediction of visual function from en face data. The 2 visual field modalities were superseded by grids with different spatial densities, resulting in a different number of visual field locations analyzed. In SAP, a median of 39 locations per participant (IQR, 37.5−40.5) were considered, with the value rising to 543.5 (IQR, 531.4−555.6) for custom perimetry.

The findings from the agreement analysis are reported in Table 2. All the participants with glaucoma showed at least 1 location where perimetry (both SAP and custom perimetry) and en face analysis were concordant on the presence of a defect. In SAP, there was a median of 3 concordant damaged locations (range, 1−9), whereas in custom perimetry, there were, on average, 82 concordant defects (median, 82; range, 20−159).

As shown in Table 2, there was moderate-to-good overall agreement between the SAP results and corresponding estimates of visual function detected using the en face analysis (median, 0.66; IQR, 0.57−0.77). Stronger agreement was found on concurrently healthy locations (negative agreement) than on concurrently abnormal areas (positive agreement) across test modalities. In fact, on average, 40% of damaged locations detected using a given test had a corresponding defect detected using the other test modality (median positive agreement, 0.40; IQR, 0.24−0.47), whereas the likelihood of both the tests corresponding on healthy locations was 77% (median negative agreement, 0.77; IQR, 0.66−0.86). Overall,

the en face analysis and SAP showed a moderate and variable correlation (median ρ, 0.34; range, −0.29 to 0.81).

Slightly stronger agreement was observed between custom perimetry and the en face predictions of visual function. On average, 68% of locations had a corresponding prediction of defect or normality (median overall agreement, 0.68; IQR, 0.60−0.76). Consistent with the SAP analysis, the agreement on defects was poorer than that on healthy locations (median positive agreement, 0.44; IQR, 0.27−0.58; median negative agreement, 0.78; IQR, 0.69−0.84). The correlation between custom perimetry findings and reflectance status across the participants was, on average, stronger compared with that between the SAP analysis and reflectance status (median ρ, 0.51; range, − 0.02 to 0.95).

The structure−function concordance between the SAP and en face analyses for each individual eye is shown in Figure 6. In total, 575 locations were assessed for SAP, and 192 showed disagreement, with abnormal en face analysis being more common than abnormal SAP (n = 116 [60.4%] vs. n = 78 [40.6%]). The findings of custom perimetry are provided in Figure S1 (available at www.ophthalmologyglaucoma.org). For custom perimetry, in all eyes with glaucoma, 2671 locations out of the 8462 assessed in total showed disagreement. Consistent with SAP, abnormal en face analysis was more frequent (n = 1563 [58.5%]) than abnormal custom perimetry (n = 1108 [41.5%]) in locations with disagreement.

Discussion

Evaluation of glaucomatous damage using en face OCT imaging is a clinically appealing and rapidly expanding area. We recently introduced a method to objectively and automatically extract reflectance defects from OCT en face images, which addressed some of the limitations of currently available methods.[23] For further validation, in this study, we explored how identified defects relate to conventional measures of glaucoma damage, such as structural changes in cpRNFLT and loss of visual function, as measured using 2 different visual field strategies. Because glaucoma frequently develops in focal patterns,[50,51] we strived to evaluate the structure−structure and structure−function relationships using a topographic and pointwise approach. This was achieved by considering concordance between individual locations of each domain, and the method used adds to the few frameworks available for pointwise comparisons across domains.[38,52−55] Such an approach may enable the consideration of the typical pattern of onset of glaucoma defects while minimizing conflation of healthy and damaged locations, reported to be among factors that can obscure structure−function relationships.[56,57]

Structure−Structure

Reflectance abnormalities showed a high level of concordance with conventional cpRNFLT loss, with 85% of en face defects having corresponding cpRNFL thinning at the mapped angular location of insertion on the ONH. The concordance ratios among the participants with glaucoma were generally high, with 1 outlier standing out from the sample (Participant 1; concordance ratio, 0.48). The SMAS
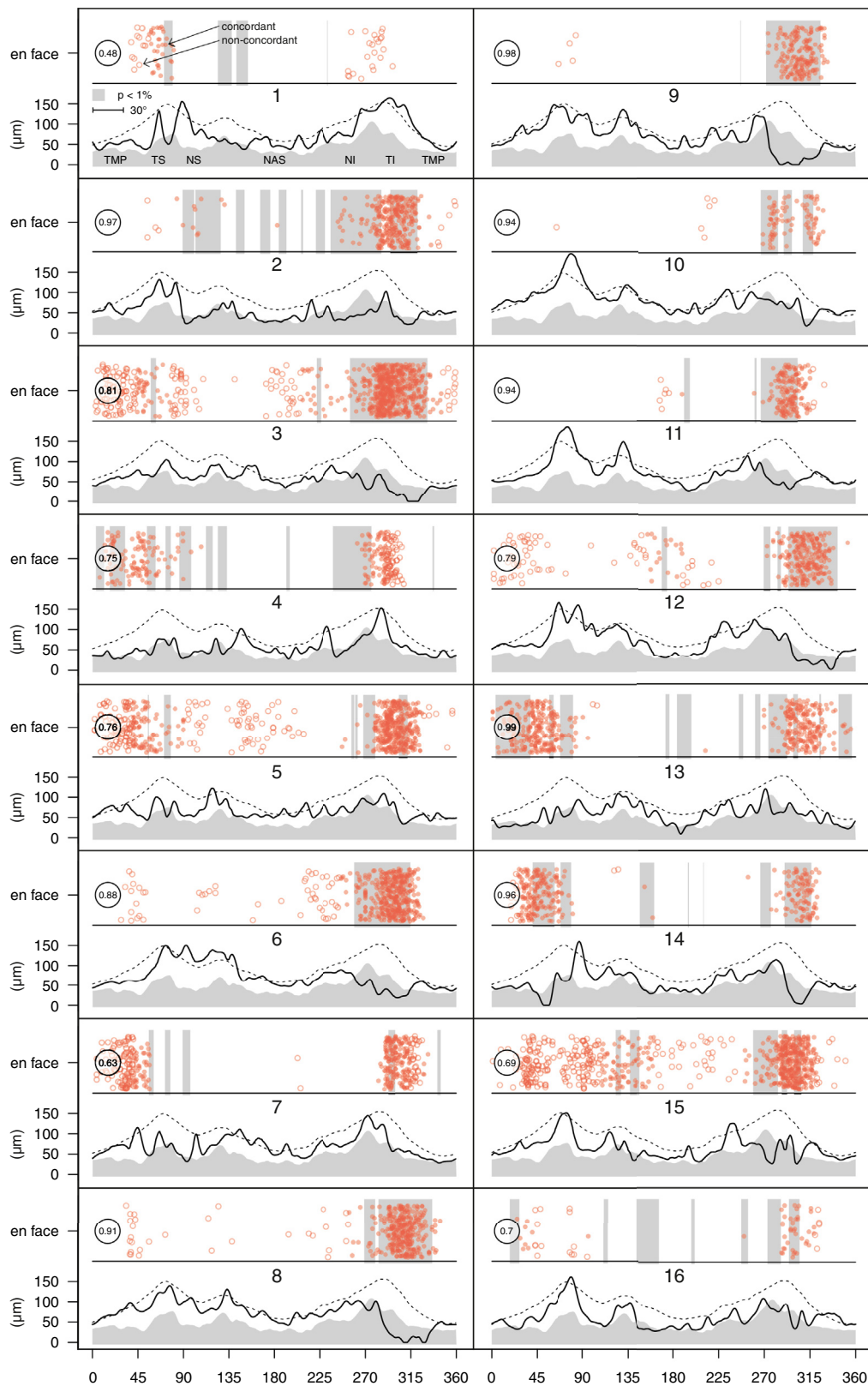
Cheloni and Denniss · Concordance of OCT Reflectance Loss with Conventional Changes in Glaucoma

Figure 4. Concordant findings between en face defects and circumpapillary retinal nerve fiber layer thickness (cpRNFLT) for all participants with glaucoma. For each participant, the bottom of the panel reports the individual cpRNFLT (black solid line) compared with age-adjusted normative data (black dashed line) and lower limit of normality ($P < 0.01$, gray area). Furthermore, cpRNFLT defects (i.e., $P < 0.01$) are found where cpRNFLT falls within the gray area and are also reported in the top of each panel as gray rectangles. En face defects found in the retina as mapped to the optic nerve head (red circles) are reported at the corresponding angle along the circumpapillary retinal nerve fiber layer profile. The filled and empty points show concordant and discordant defects, respectively. The concordance ratio for each participant is also reported in the top left corner of each subplot.
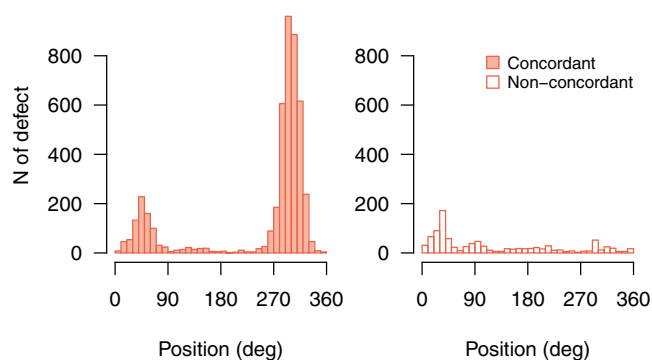
Figure 5. Distributions of angular insertions on the optic nerve head as mapped by the model adopted in this study.[34] Data are shown separately for concordant en face defects (left plot, mode = 297°) and abnormal superpixels without corresponding circumpapillary retinal nerve fiber layer defect (right plot, mode = 38°). deg = degree.

deviation maps of this participant and the first 4 slabs feeding SMAS are shown in Figure 7.

The objective analysis of reflectance helped identify a narrow, superior arcuate defect and a number of abnormal superpixels in the inferior nasal quadrant (23 out of the total 67 abnormal superpixels). Yet, abnormalities found in the inferior retina were likely due to artifacts, and this quadrant overall appeared spared by glaucomatous damage in the subjective evaluation of the en face images. The integrity of the inferior nasal retina was also suggested by the cpRNFLT analysis (Fig 4, top left panel), where only superior temporal thinning was observed. It is possible that this scattered noise in the inferior hemisphere and a nonsubstantial loss of reflectance in the superior hemisphere according to the SMAS objective analysis explain the low concordance ratio found in this participant. For the same participant, a concordance ratio of 0.73 was computed by excluding

abnormal locations in the inferior nasal region, and future improvements in image capture and processing could contribute to reducing the impact on this and similar issues.

The findings of the structure−structure analysis are consistent with the available literature, showing OCT measures of reflectance loss to be strongly related to thinning of the RNFL.[8,58−60] Ashimatey et al[8] objectively evaluated reflectance defects on wide-field en face images and related them to cpRNFLT. In that study, the ratios of en face reflectance defects in the superior and inferior retinal hemispheres were strongly related with the depth of cpRNFLT defects at corresponding ONH sectors.[8] The observed strong concordance is also consistent with the generally high topographic correlation between structural measurements of glaucoma loss at the ONH (cpRNFL) and macula.[61−64] Overall, these findings suggest that in patients with established glaucoma, loss of reflectance may be well represented using the cpRNFLT analysis. This underlines the need to further evaluate the value of RNFL reflectance analyses at the earliest stage of the disease and/or in combination with perimetry. Similarly, the value of en face reflectance analysis deserves further evaluation in more advanced cases to explore any added value in overcoming cpRNFLT floor effects.[65]

Structure−Function

Overall, there was moderate-to-good agreement between the en face measures and visual field status, more strongly driven by agreement on healthy locations rather than by agreement on defects. The participants with glaucoma showed, on average, 3 and 82 concordant defects using SAP and custom perimetry, respectively. Similar measures were not computed in the controls because the inclusion criteria required normal visual field by definition, and no abnormal superpixels were detected in healthy eyes. Although

Table 2. Findings from Agreement Analysis for Standard Automated Perimetry and Custom Perimetry*

	SAP (Defect If Total Deviation with P < 0.02)				Custom Perimetry			
Participant	*Overall*	*Positive*	*Negative*	*P Value*	*Overall*	*Positive*	*Negative*	*P Value*
1	0.69 (0.58−0.82)	0.36 (0.11−0.62)	0.79 (0.70−0.91)	0.021	0.76 (0.72−0.79)	0.22 (0.15−0.30)	0.85 (0.83−0.88)	< 0.0001
2	0.55 (0.40−0.71)	0.24 (0.01−0.48)	0.68 (0.55−0.83)	0.72	0.61 (0.56−0.65)	0.42 (0.36−0.48)	0.70 (0.66−0.74)	0.004
3	0.58 (0.42−0.74)	0.53 (0.33−0.76)	0.62 (0.46−0.82)	0.15	0.64 (0.60−0.68)	0.62 (0.57−0.67)	0.66 (0.62−0.71)	< 0.0001
4	0.51 (0.35−0.68)	0.25 (0.01−0.50)	0.64 (0.50−0.81)	0.71	0.57 (0.53−0.61)	0.40 (0.33−0.46)	0.66 (0.62−0.70)	0.15
5	0.42 (0.27−0.58)	0.10 (0.01−0.19)	0.58 (0.42−0.77)	0.58	0.44 (0.40−0.48)	0.20 (0.14−0.26)	0.57 (0.53−0.62)	0.89
6	0.85 (0.76−0.98)	0.67 (0.45−1.00)	0.91 (0.84−1.00)	0.001	0.83 (0.80−0.87)	0.72 (0.66−0.78)	0.88 (0.86−0.90)	< 0.0001
7	0.63 (0.47−0.79)	0.12 (0.01−0.25)	0.77 (0.65−0.91)	1	0.58 (0.54−0.63)	0.21 (0.14−0.28)	0.72 (0.68−0.76)	1
8	0.79 (0.68−0.92)	0.43 (0.14−0.86)	0.87 (0.79−0.98)	0.048	0.85 (0.82−0.88)	0.73 (0.68−0.79)	0.89 (0.87−0.92)	< 0.0001
9	0.82 (0.71−0.95)	0.46 (0.15−0.92)	0.89 (0.82−0.98)	0.063	0.92 (0.89−0.94)	0.82 (0.78−0.88)	0.94 (0.93−0.96)	< 0.0001
10	0.76 (0.63−0.90)	0.17 (0.01−0.33)	0.86 (0.78−0.96)	1	0.74 (0.70−0.77)	0.39 (0.31−0.47)	0.83 (0.80−0.86)	< 0.0001
11	0.55 (0.32−0.73)	0.38 (0.05−0.75)	0.64 (0.46−0.89)	1	0.68 (0.63−0.73)	0.29 (0.19−0.40)	0.79 (0.75−0.83)	0.009
12	0.77 (0.64−0.90)	0.40 (0.13−0.80)	0.86 (0.77−0.95)	0.024	0.76 (0.73−0.80)	0.57 (0.50−0.64)	0.84 (0.81−0.87)	< 0.0001
13	0.63 (0.49−0.78)	0.48 (0.28−0.73)	0.72 (0.60−0.88)	0.30	0.51 (0.47−0.55)	0.53 (0.48−0.58)	0.49 (0.43−0.54)	0.49
14	0.71 (0.57−0.86)	0.40 (0.13−0.69)	0.81 (0.72−0.94)	0.21	0.69 (0.65−0.73)	0.54 (0.48−0.60)	0.77 (0.74−0.81)	< 0.0001
15	0.62 (0.48−0.80)	0.48 (0.28−0.74)	0.71 (0.57−0.87)	0.3	0.63 (0.59−0.67)	0.47 (0.41−0.53)	0.72 (0.68−0.76)	< 0.0001
16	−	−	−	−	0.72 (0.68−0.76)	0.23 (0.15−0.32)	0.83 (0.80−0.86)	0.074

SAP = standard automated perimetry.
*Values of overall, positive, and negative agreements are reported with their bootstrapped 95% confidence intervals. *P* values for Fisher exact tests for independence of the 2 test modalities in the overall agreement analysis are also reported.
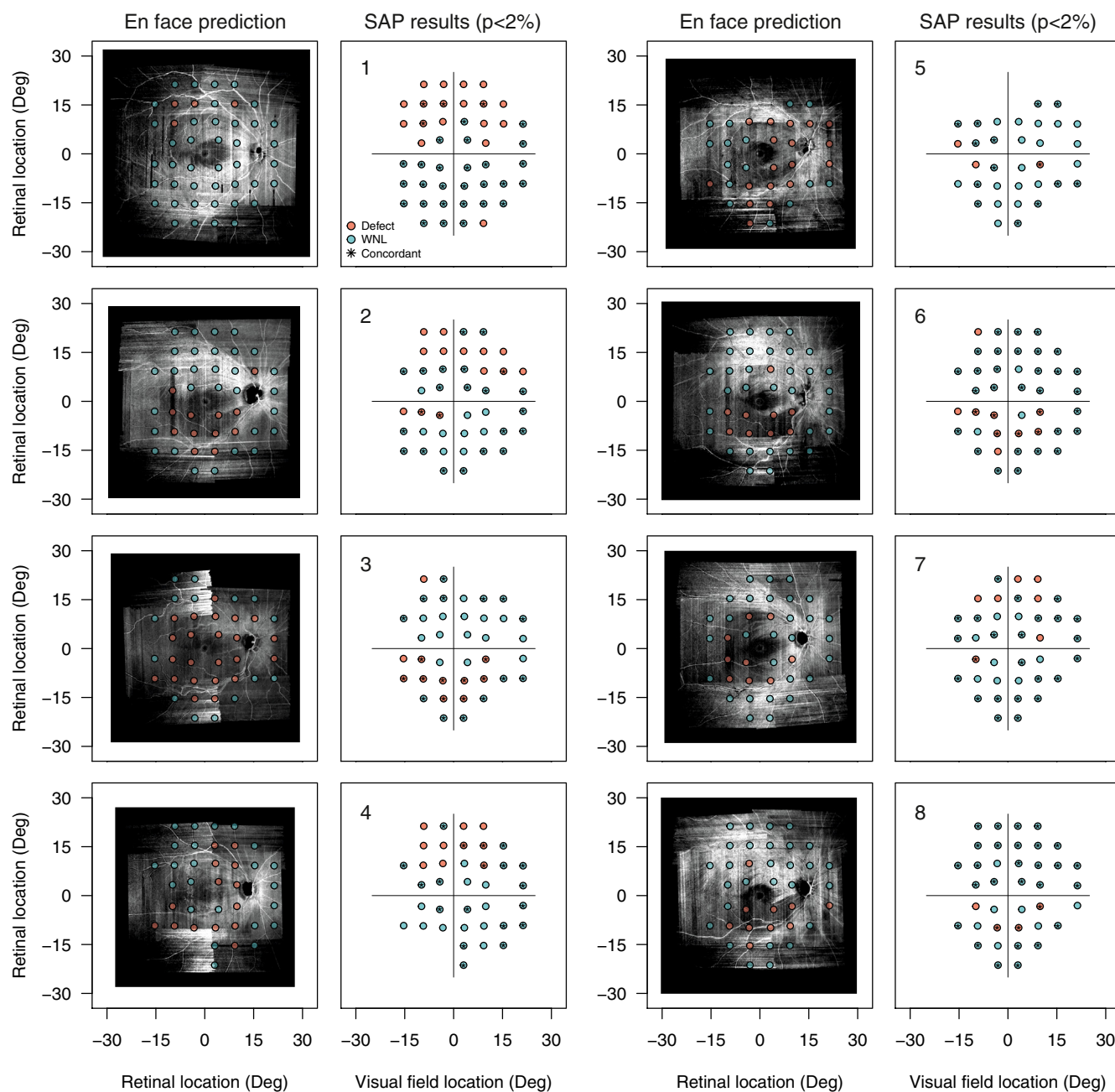
Figure 6. Correspondence between en face predictions of visual function and dichotomized standard automated perimetry results. The en face predictions of visual field status are overlaid on the en face image of the patient; locations are color coded as the observed status for each test domain, and locations where there was en face–standard automated perimetry agreement are flagged with asterisks (figure continues on to the next page). Deg = degree; SAP = standard automated perimetry; WNL = within normal limits.

concordance was imperfect, all eyes with glaucoma showed some levels of structure–function agreement on the presence of abnormalities, and the ability of similar concordance thresholds for glaucoma detection deserves further investigation.

The sources of disagreement between the en face and SAP findings were qualitatively explored post hoc (Table S2, available at www.ophthalmologyglaucoma.org). In up to 53% (9/17) of hemispheres with imperfect agreement, en

face defects did not match with SAP defects. Yet, in 5 of these cases, artifacts contributed at least in part to abnormal reflectivity, leading to imperfect agreement. The remaining 4 hemispheres could instead suggest that reflectance loss preceded visual field changes; however, further validation in cohorts of larger sample sizes is required. Standard automated perimetry defects and normal reflectivity were observed in 23.5% (4/17) of cases with poor agreement. However, in 3 out of the 4 cases, reflectance loss could be
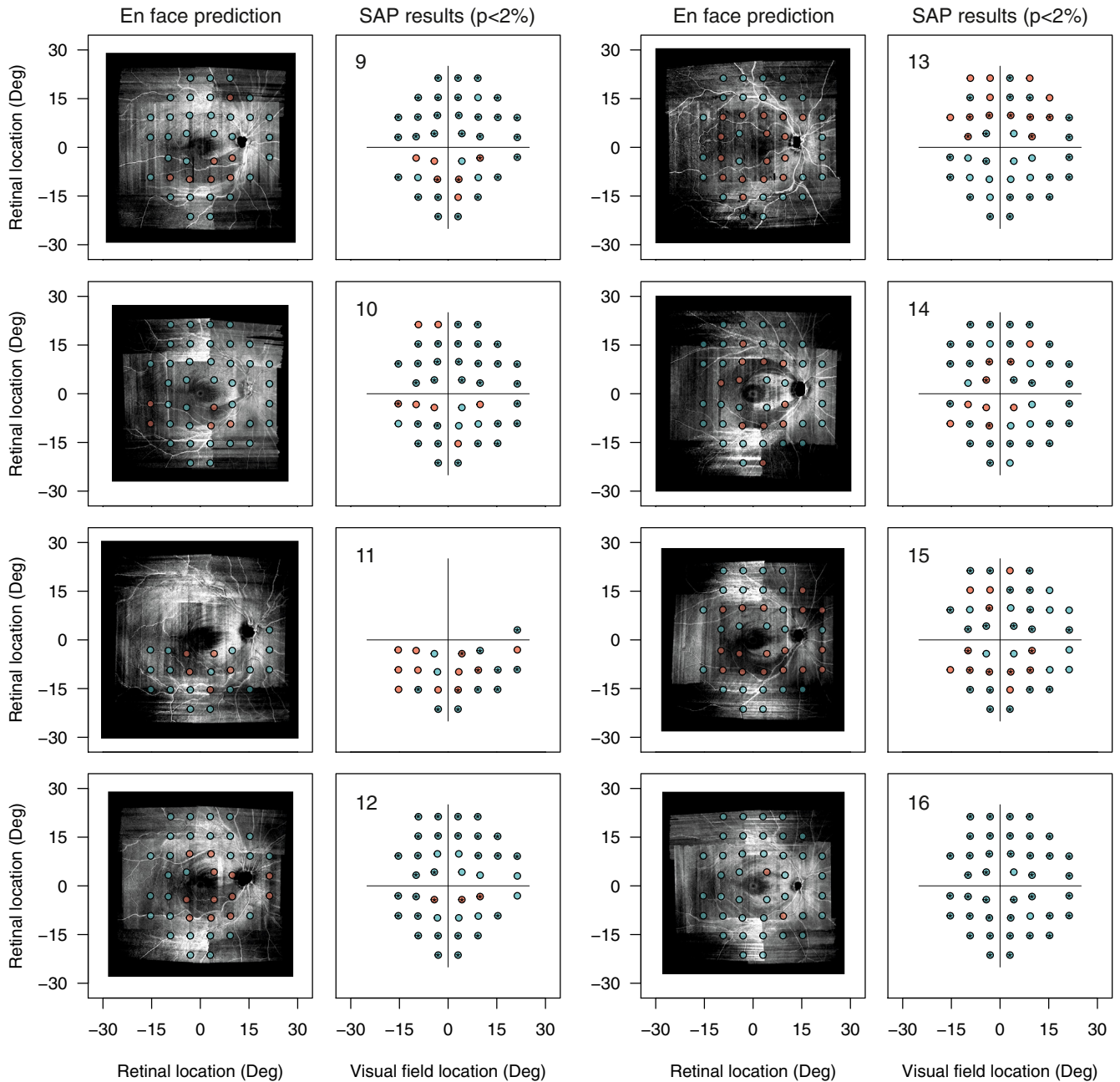
Figure 6. (*continued*).

observed subjectively on the en face images, and further refinement of the SMAS analysis could result in stronger concordance. In a few hemispheres (23.5%), both the domains showed defects, and imperfect spatial overlap seems to explain this disagreement.

Besides genuinely different time scales at which en face reflectance and visual field could be affected in patients with glaucoma, several reasons might contribute to disagreement between the 2 domains. As discussed above, RGC displacement and eye movements may be a potential confounder in this relationship, and we aimed to control for their impact by

allowing a 1° tolerance around visual field locations. In addition, visual field stimuli could be presented at the border of a scotoma, or the location tested could still have preserved RGCs but not visible or measurable RNFBs with the imaging device used. Anomalously high or low hills of vision for specific participants should also be considered. Apart from potential sources of disagreement, it should also be noted that every structural defect may not necessarily correspond to a visual field defect and vice versa. In fact, the RNFL represents only 1 part of the whole visual pathway, which may fail to capture other consequences of glaucoma.[66,67] Similarly, there may be

A

B

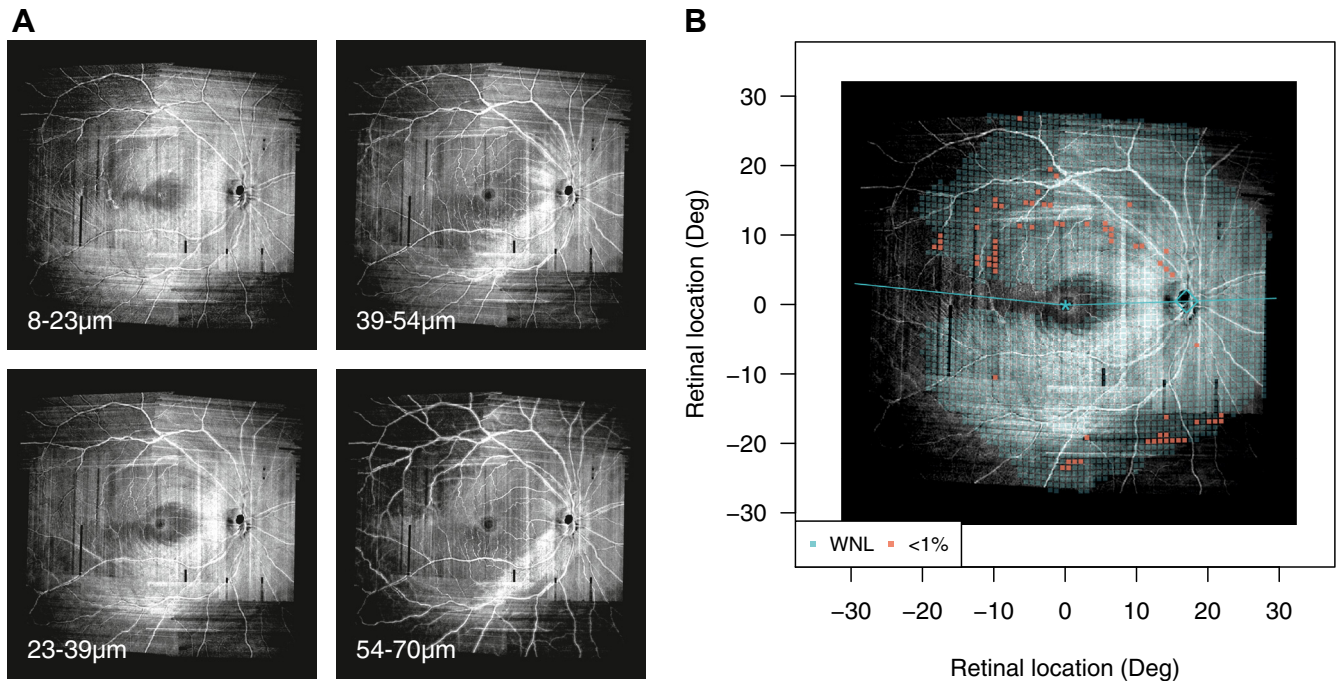**Figure 7. A,** En face slab images (first 4 slabs out of the 7 considered in the Summary of Multiple Anatomically-adjusted Slabs analysis). The corresponding depth below the inner limiting membrane, considered by each single slab is reported in micrometers. **B,** Summary of Multiple Anatomically-adjusted Slabs deviation map. Deg = degree; WNL = within normal limits.

compensatory mechanisms leading to minimally impacted visual function in the presence of structural glaucoma damage.[68,69]

Consistent with our results, studies exploring the relationship between reflectance loss and visual function have generally shown good agreement.[12,17,18,20,21,70] Earlier work by Alluwimi et al[17,20] examined the central retina of 10 eyes with glaucoma using en face imaging and the corresponding function using a customized visual field. Consistent with our analysis, the authors found good concordance between the 2 domains, stronger for normal findings (74%−90% agreement) than for damaged locations (31%−48% agreement).[17] In more recent work,[18] the same group used kinetic perimetry to explore visual function along reflectance defects connected to the ONH. They showed spatial correspondence between en face and functional defects, which, consistent with en face abnormalities, were always connected to the ONH.[18] Even stronger agreement was observed by Iikawa et al[21] in a study that superimposed SAP 10-2 results on macular en face images. Here, the presence or absence of RNFBs underneath visual field locations correctly predicted ∼ 85% of locations to be either defective or normal. Lastly, Sakamoto et al[12] focused on eyes with advanced glaucoma and evaluated the concordance between preserved RNFBs on en face macula images and SAP 10-2. The authors concluded that preserved bundles and function had a high level of agreement; however, little detail was provided on specific instruction and/or criteria adopted by the clinicians to establish preserved reflectance and agreement itself.

The common features of previous studies were focus on the macular region and the use of subjective methods for the assessment of reflectivity and concordance. Subjective analyses of reflectance are likely to be less prone to image artifacts and yet have limitations in terms of practicality, technique standardization, and selection bias due to pre-conceived expectations of RNFB defects. Additionally, when correspondence with the visual field is evaluated subjectively, a variable level of tolerance in spatial agreement could be present in different locations and different eyes, hampering consistency compared with the more objective approach of the present study.

This study has some limitations. The conversion of the en face images from superpixels to degrees relied on different scans (Spectralis Glaucoma Module vs. wide-field montage) and different methods for the identification of the distance between the fovea and the ONH (automated by the Spectralis software vs. subjective en face analysis). Inaccuracies in detection of anatomic structures and changes in eye position, rotation, and scaling across the scans could have led to imprecise mapping of structural data to visual field results. However, we expect this source of error to be small and controlled for by the tolerance levels used in the structure−structure and structure−function analyses. Additionally, our assessment of structure−structure and structure−function concordance required us to set pre-determined cutoffs to establish defects in all domains. The observed levels of concordance in this study likely depend to a certain extent on the thresholds set and the choice of whether or not to adjust for overall changes in reflectance and visual field sensitivity before looking for local defects. Further analyses could be conducted to refine defect definitions for optimal agreement, as proposed elsewhere.[53]

Our inclusion criteria for the participants with glaucoma, based solely on structural defects, could have allowed the

inclusion of healthy eyes in the group of participants with glaucoma.[71] However, all our participants with glaucoma, except 1, presented with a visual field defect. This, combined with the requirement of a glaucoma diagnosis by a consultant ophthalmologist, means that it is unlikely that our sample was significantly influenced by false-positive glaucoma cases.

Our analysis of cpRNFLT included age correction, as planned from the outset. However, given the narrow age range in our sample, the greatest cpRNFLT correction was 3.1 μm. This value was below the OCT digital axial resolution and, therefore, unlikely to have affected the results. As such, age correction may not be necessary for future studies with a similar age range of participants.

Lastly, as also discussed previously,[23] the artifacts of en face imaging had considerable impact on the objective analysis of reflectance using SMAS. Future improvements in en face image capture and processing should focus on several areas, including the following: (1) better strategies to correct for uneven intensities of different scans and (2) enhanced ability to detect reflectance defects, especially in the superior and inferior arcuate regions of wide-field images and in the nasal step area. Among many strategies, the consideration of the distance between vascular arcades and the fovea would represent a variable for evaluation while adjusting for individual anatomy because this could also affect the configuration of RNFBs across the retina.[72] Reduction in the variability of reflectance data in healthy eyes, achieved by addressing en face artifacts, would also likely result in improved capability to detect defects. Further study in this area would be beneficial to address the many remaining gaps. Studies on larger groups of healthy eyes would enable us to better determine normative limits, reducing the risk of misclassification of defects. Larger studies would also allow us to explore the impact of different covariates on reflectance values, such as age, axial length, and ethnicity.[58,73,74]

In summary, this study further validated the SMAS analysis of en face images by establishing correspondence between reflectance abnormalities and conventional measures of glaucoma damage. A framework for objectively assessing pointwise relationships between structure−structure and structure−function was introduced. The majority of retinal locations with abnormal reflectance presented a matched cpRNFLT defect at the estimated insertion on the ONH. The agreement between the en face analysis and visual field data was moderate to good, and further minimization of artifacts in en face imaging could lead to stronger concordance. All the participants showed a number of locations with abnormal reflectivity and function, and the diagnostic capability of similar criteria to detect early stages of glaucoma deserves dedicated assessment. Stronger agreement was found between regions with normal reflectivity and preserved visual function, and this property could be exploited to drive custom perimetry strategies in eyes with advanced glaucoma, aiming to monitor disease progression in areas that can provide more reliable functional data. Further evaluation in representative samples with relevant stages of glaucoma is warranted.

Footnotes and Disclosures

Correspondence:

Jonathan Denniss, PhD, School of Optometry & Vision Science, University of Bradford, Richmond Road, Bradford BD7 1DP, United Kingdom. E-mail: j.denniss@bradford.ac.uk.

References

1. Tatham AJ, Medeiros FA, Zangwill LM, Weinreb RN. Strategies to improve early diagnosis in glaucoma. *Prog Brain Res*. 2015;221:103−133.

2. World Glaucoma Association. In: Weinreb RN, Garway-Heath DF, Leung C, Medeiros FA, Liebmann J, eds.*10th Consensus Meeting: Diagnosis of Primary Open Angle Glaucoma*. Seattle, WA: Kugler Publications; 2016:.

3. Jindal A, Ctori I, Fidalgo B, et al. Impact of optical coherence tomography on diagnostic decision-making by UK community optometrists: a clinical vignette study. *Ophthalmic Physiol Opt*. 2019;39:205−215.

4. Founti P, Coleman AL, Wilson MR, et al. Overdiagnosis of open-angle glaucoma in the general population: the Thessaloniki Eye Study. *Acta Ophthalmol*. 2018;96:e859−e864.

5. Michelessi M, Li T, Miele A, et al. Accuracy of optical coherence tomography for diagnosing glaucoma: an overview of systematic reviews. *Br J Ophthalmol*. 2021;105: 490−495.

6. Virgili G, Michelessi M, Cook J, et al. Diagnostic accuracy of optical coherence tomography for diagnosing glaucoma: secondary analyses of the GATE study. *Br J Ophthalmol*. 2018;102:604−610.

7. Stagg BC, Medeiros FA. A comparison of OCT parameters in identifying glaucoma damage in eyes suspected of having glaucoma. *Ophthalmol Glaucoma*. 2020;3:90−96.

8. Ashimatey BS, King BJ, Burns SA, Swanson WH. Evaluating glaucomatous abnormality in peripapillary optical coherence tomography enface visualisation of the retinal nerve fibre layer reflectance. *Ophthalmic Physiol Opt*. 2018;38:376−388.

9. Hood DC, Fortune B, Mavrommatis MA, et al. Details of glaucomatous damage are better seen on OCT en face images than on OCT retinal nerve fiber layer thickness maps. *Invest Ophthalmol Vis Sci*. 2015;56:6208−6216.

10. King BJ, Swanson WH, Klemencic SA, et al. Assessing the impact of en face retinal nerve fiber layer imaging on clinical decision making for glaucoma suspects. *Optom Vis Sci*. 2020;97:54−61.

11. Cheloni R, Dewsbery SD, Denniss J. A simple subjective evaluation of enface OCT reflectance images distinguishes glaucoma from healthy eyes. *Transl Vis Sci Technol*. 2021;10, 31−31.

12. Sakamoto M, Mori S, Ueda K, et al. En face slab images visualize nerve fibers with residual visual sensitivity in significantly thinned macular areas of advanced glaucomatous eyes. *Invest Ophthalmol Vis Sci*. 2019;60:2811−2821.

13. Mavrommatis MA, De Cuir N, Reynaud J, et al. An examination of the frequency of paravascular defects and epiretinal membranes in eyes with early glaucoma using en-face slab OCT images. *J Glaucoma*. 2019;28:265−269.

14. Huang XR, Zhou Y, Kong W, Knighton RW. Reflectance decreases before thickness changes in the retinal nerve fiber layer in glaucomatous retinas. *Invest Ophthalmol Vis Sci*. 2011;52:6737−6742.

15. Liu S, Wang B, Yin B, et al. Retinal nerve fiber layer reflectance for early glaucoma diagnosis. *J Glaucoma*. 2014;23: e45−e52.

16. Fortune B, Burgoyne CF, Cull G, et al. Onset and progression of peripapillary retinal nerve fiber layer (RNFL) retardance changes occur earlier than RNFL thickness changes in experimental glaucoma. *Invest Ophthalmol Vis Sci*. 2013;54: 5653−5661.

17. Alluwimi MS, Swanson WH, Malinovsky VE, King BJ. Customizing perimetric locations based on en face images of retinal nerve fiber bundles with glaucomatous damage. *Transl Vis Sci Technol*. 2018;7:5.

18. Ashimatey BS, King BJ, Swanson WH. Functional characteristics of glaucoma related arcuate defects seen on OCT en face visualisation of the retinal nerve fibre layer. *Ophthalmic Physiol Opt*. 2021;41:437−446.

19. Denniss J, Turpin A, McKendrick AM. Relating optical coherence tomography to visual fields in glaucoma: structure-function mapping, limitations and future applications. *Clin Exp Optom*. 2019;102:291−299.

20. Alluwimi MS, Swanson WH, Malinovsky VE, King BJ. A basis for customising perimetric locations within the macula in glaucoma. *Ophthalmic Physiol Opt*. 2018;38:164−173.

21. Iikawa R, Togano T, Sakaue Y, et al. Estimation of the central 10-degree visual field using en-face images obtained by optical coherence tomography. *PLoS One*. 2020;15, e0229867.

22. Cheloni R, Denniss J. Depth-resolved variations in visibility of retinal nerve fibre bundles across the retina in enface OCT images of healthy eyes. *Ophthalmic Physiol Opt*. 2021;41: 179−191.

23. Cheloni R, Dewsbery SD, Denniss J. Enhanced objective detection of retinal nerve fiber bundle defects in glaucoma with a novel method for en face OCT slab image construction and analysis. *Transl Vis Sci Technol*. 2021;10:1.

24. Chylack LT, Wolfe JK, Singer DM, et al. The lens opacities classification system III. *Arch Ophthalmol*. 1993;111: 831−836.

25. Vermeer KA, Mo J, Weda JJ, et al. Depth-resolved model-based reconstruction of attenuation coefficients in optical coherence tomography. *Biomed Opt Express*. 2013;5: 322−337.

26. Realini T, Zangwill L, Flanagan J, et al. Normative databases for imaging instrumentation. *J Glaucoma*. 2015;24:480−483.

27. Green SB. How many subjects does it take to do a regression analysis. *Multivariate Behav Res*. 1991;26:499−510.

28. Wang M, Elze T, Li D, et al. Age, ocular magnification, and circumpapillary retinal nerve fiber layer thickness. *J Biomed Opt*. 2017;22, 121718.

29. Turpin A, Artes PH, McKendrick AM. The Open Perimetry Interface: an enabling tool for clinical visual psychophysics. *J Vis*. 2012;12:22.

30. Heijl A, Lindgren G, Olsson J. Normal variability of static perimetric threshold values across the central visual field. *Arch Ophthalmol*. 1987;105:1544−1549.

31. Henson DB, Artes PH, Chaudry SJ, Chauhan BC. Supra-threshold perimetry: establishing the test intensity. *Ophthalmic Physiol Opt*. 1995;15:243−252.

32. Henson DB, Artes PH. New developments in supra-threshold perimetry. *Ophthalmic Physiol Opt*. 2002;22:463−468.

33. Patel DE, Cumberland PM, Walters BC, et al. Study of Optimal Perimetric Testing in Children (OPTIC): feasibility, reliability and repeatability of perimetry in children. *PLoS One*. 2015;10, e0130895.

34. Denniss J, McKendrick AM, Turpin A. An anatomically customizable computational model relating the visual field to the optic nerve head in individual eyes. *Invest Ophthalmol Vis Sci*. 2012;53:6981−6990.

35. Denniss J, Turpin A, McKendrick AM. Individualized structure-function mapping for glaucoma: practical constraints

on map resolution for clinical and research applications. *Invest Ophthalmol Vis Sci*. 2014;55:1985−1993.

36. Denniss J, Turpin A, Tanabe F, et al. Structure-function mapping: variability and conviction in tracing retinal nerve fiber bundles and comparison to a computational model. *Invest Ophthalmol Vis Sci*. 2014;55:728−736.

37. McKendrick AM, Denniss J, Wang YX, et al. The proportion of individuals likely to benefit from customized optic nerve head structure-function mapping. *Ophthalmology*. 2017;124:554−561.

38. Turpin A, McKendrick AM. Improving personalized structure to function mapping from optic nerve head to visual field. *Transl Vis Sci Technol*. 2021;10:19.

39. Drasdo N, Millican CL, Katholi CR, Curcio CA. The length of Henle fibers in the human retina and a model of ganglion receptive field density in the visual field. *Vision Res*. 2007;47:2901−2911.

40. Ashimatey BS, King BJ, Swanson WH. Retinal putative glial alterations: implication for glaucoma care. *Ophthalmic Physiol Opt*. 2018;38:56−65.

41. Montesano G, Rossetti LM, Allegrini D, et al. Improving visual field examination of the macula using structural information. *Transl Vis Sci Technol*. 2018;7:36.

42. Montesano G, Rossetti LM, Allegrini D, et al. Systematic and random mapping errors in structure−function analysis of the macula. *Transl Vis Sci Technol*. 2021;10, 21−21.

43. Turpin A, Chen S, Sepulveda JA, McKendrick AM. Customizing structure-function displacements in the macula for individual differences. *Invest Ophthalmol Vis Sci*. 2015;56:5984−5989.

44. Drasgow F. Polychoric and polyserial correlations. In: Balakrishnan N, Colton T, Everitt B, Piegorsch W, Ruggeri F, Teugels JL, eds. *Wiley StatsRef: Statistics Reference Online*. Hoboken, NJ: Wiley; 2014:68−74.

45. Olsson U. Maximum likelihood estimation of the polychoric correlation coefficient. *Psychometrika*. 1979;44:443−460.

46. Makowski D, Ben-Shachar MS, Patil I, Lüdecke D. Methods and algorithms for correlation analysis in R. *J Open Source Softw*. 2020;5:2306.

47. Uebersax JS. Diversity of decision-making models and the measurement of interrater agreement. *Psychol Bull*. 1987;101:140−146.

48. Cicchetti DV, Feinstein AR. High agreement but low kappa: II. Resolving the paradoxes. *J Clin Epidemiol*. 1990;43:551−558.

49. Spitzer RL, Fleiss JL. A re-analysis of the reliability of psychiatric diagnosis. *Br J Psychiatry*. 1974;125:341−347.

50. Nicolela MT, Drance SM. Various glaucomatous optic nerve appearances: clinical correlations. *Ophthalmology*. 1996;103:640−649.

51. Elze T, Pasquale LR, Shen LQ, et al. Patterns of functional vision loss in glaucoma determined with archetypal analysis. *J R Soc Interface*. 2015;12, 20141118.

52. Ganeshrao SB, Turpin A, Denniss J, McKendrick AM. Enhancing structure-function correlations in glaucoma with customized spatial mapping. *Ophthalmology*. 2015;122:1695−1705.

53. Tsamis E, Bommakanti NK, Sun A, et al. An automated method for assessing topographical structure−function agreement in abnormal glaucomatous regions. *Transl Vis Sci Technol*. 2020;9:14.

54. Hirasawa K, Matsuura M, Fujino Y, et al. Comparing structure-function relationships based on Drasdo's and Sjöstrand's retinal ganglion cell displacement models. *Invest Ophthalmol Vis Sci*. 2020;61:10.

55. Mohammadzadeh V, Rabiolo A, Fu Q, et al. Longitudinal macular structure-function relationships in glaucoma. *Ophthalmology*. 2020;127:888−900.

56. Araie M, Saito H, Tomidokoro A, et al. Relationship between macular inner retinal layer thickness and corresponding retinal sensitivity in normal eyes. *Invest Ophthalmol Vis Sci*. 2014;55:7199−7205.

57. Chu FI, Marin-Franch I, Ramezani K, Racette L. Associations between structure and function are different in healthy and glaucomatous eyes. *PLoS One*. 2018;13, e0196814.

58. Thepass G, Lemij HG, Vermeer KA. Attenuation coefficients from SD-OCT data: structural information beyond morphology on RNFL integrity in glaucoma. *J Glaucoma*. 2017;26:1001−1009.

59. Pons ME, Ishikawa H, Gürses-Ozden R, et al. Assessment of retinal nerve fiber layer internal reflectivity in eyes with and without glaucoma using optical coherence tomography. *Arch Ophthalmol*. 2000;118:1044−1047.

60. Tan O, Liu L, You Q, et al. Focal loss analysis of nerve fiber layer reflectance for glaucoma diagnosis. *Transl Vis Sci Technol*. 2021;10:9.

61. Kim KE, Park KH. Macular imaging by optical coherence tomography in the diagnosis and management of glaucoma. *Br J Ophthalmol*. 2018;102:718−724.

62. Shin HY, Park HY, Jung KI, Park CK. Comparative study of macular ganglion cell-inner plexiform layer and peripapillary retinal nerve fiber layer measurement: structure-function analysis. *Invest Ophthalmol Vis Sci*. 2013;54:7344−7353.

63. Kim KE, Park KH, Yoo BW, et al. Topographic localization of macular retinal ganglion cell loss associated with localized peripapillary retinal nerve fiber layer defect. *Invest Ophthalmol Vis Sci*. 2014;55:3501−3508.

64. Wollstein G, Schuman JS, Price LL, et al. Optical coherence tomography (OCT) macular and peripapillary retinal nerve fiber layer measurements and automated visual fields. *Am J Ophthalmol*. 2004;138:218−225.

65. Bowd C, Zangwill LM, Weinreb RN, et al. Estimating optical coherence tomography structural measurement floors to improve detection of progression in advanced glaucoma. *Am J Ophthalmol*. 2017;175:37−44.

66. Frezzotti P, Giorgio A, Motolese I, et al. Structural and functional brain changes beyond visual system in patients with advanced glaucoma. *PLoS One*. 2014;9, e105931.

67. Frezzotti P, Giorgio A, Toto F, et al. Early changes of brain connectivity in primary open angle glaucoma. *Hum Brain Mapp*. 2016;37:4581−4596.

68. Bham HA, Dewsbery SD, Denniss J. Unaltered perception of suprathreshold contrast in early glaucoma despite sensitivity loss. *Invest Ophthalmol Vis Sci*. 2020;61, 23−23.

69. Bham HA, Denniss J. Effects of glaucoma on detection and discrimination of image blur. *Ophthalmic Physiol Opt*. 2022;42:471−481.

70. Christopher M, Bowd C, Belghith A, et al. Deep learning approaches predict glaucomatous visual field damage from OCT optic nerve head en face images and retinal nerve fiber layer thickness maps. *Ophthalmology*. 2020;127:346−356.

71. Chong GT, Lee RK. Glaucoma versus red disease: imaging and glaucoma diagnosis. *Curr Opin Ophthalmol*. 2012;23:79−88.

72. Varma R, Skaf M, Barron E. Retinal nerve fiber layer thickness in normal human eyes. *Ophthalmology*. 1996;103:2114−2119.

73. Mauschitz MM, Bonnemaijer PW, Diers K, et al. Systemic and ocular determinants of peripapillary retinal nerve fiber layer thickness measurements in the European eye epidemiology (E3) population. *Ophthalmology*. 2018;125:1526−1536.

74. Wagner FM, Hoffmann EM, Nickels S, et al. Peripapillary retinal nerve fiber layer profile in relation to refractive error and axial length: results from the Gutenberg Health Study. *Transl Vis Sci Technol*. 2020;9:35.